Hitomi observations of the LMC SNR N 132 D: Highly redshifted X-ray emission from iron ejecta*

Hitomi Collaboration, Felix Aharonian,[1,2,3] Hiroki Akamatsu,[4]
Fumie Akimoto,[5] Steven W. Allen,[6,7,8] Lorella Angelini,[9] Marc Audard,[10]
Hisamitsu Awaki,[11] Magnus Axelsson,[12] Aya Bamba,[13,14]
Marshall W. Bautz,[15] Roger Blandford,[6,7,8] Laura W. Brenneman,[16]
Gregory V. Brown,[17] Esra Bulbul,[15] Edward M. Cackett,[18]
Maria Chernyakova,[1] Meng P. Chiao,[9] Paolo S. Coppi,[19,20]
Elisa Costantini,[4] Jelle de Plaa,[4] Cor P. de Vries,[4] Jan-Willem den Herder,[4]
Chris Done,[21] Tadayasu Dotani,[22] Ken Ebisawa,[22] Megan E. Eckart,[9]
Teruaki Enoto,[23,24] Yuichiro Ezoe,[25] Andrew C. Fabian,[26] Carlo Ferrigno,[10]
Adam R. Foster,[16] Ryuichi Fujimoto,[27] Yasushi Fukazawa,[28]
Akihiro Furuzawa,[29] Massimiliano Galeazzi,[30] Luigi C. Gallo,[31]
Poshak Gandhi,[32] Margherita Giustini,[4] Andrea Goldwurm,[33,34] Liyi Gu,[4]
Matteo Guainazzi,[35] Yoshito Haba,[36] Kouichi Hagino,[37]
Kenji Hamaguchi,[9,38] Ilana M. Harrus,[9,38] Isamu Hatsukade,[39]
Katsuhiro Hayashi,[22,40] Takayuki Hayashi,[40] Kiyoshi Hayashida,[41]
Junko S. Hiraga,[42] Ann Hornschemeier,[9] Akio Hoshino,[43]
John P. Hughes,[44] Yuto Ichinohe,[25] Ryo Iizuka,[22] Hajime Inoue,[45]
Yoshiyuki Inoue,[22] Manabu Ishida,[22] Kumi Ishikawa,[22] Yoshitaka Ishisaki,[25]
Masachika Iwai,[22] Jelle Kaastra,[4,46] Tim Kallman,[9] Tsuneyoshi Kamae,[13]
Jun Kataoka,[47] Satoru Katsuda,[48] Nobuyuki Kawai,[49] Richard L. Kelley,[9]
Caroline A. Kilbourne,[9] Takao Kitaguchi,[28] Shunji Kitamoto,[43]
Tetsu Kitayama,[50] Takayoshi Kohmura,[37] Motohide Kokubun,[22]
Katsuji Koyama,[51] Shu Koyama,[22] Peter Kretschmar,[52] Hans A. Krimm,[53,54]
Aya Kubota,[55] Hideyo Kunieda,[40] Philippe Laurent,[33,34] Shiu-Hang Lee,[23]
Maurice A. Leutenegger,[9,38] Olivier Limousin,[34] Michael Loewenstein,[9,56]
Knox S. Long,[57] David Lumb,[35] Greg Madejski,[6] Yoshitomo Maeda,[22]
Daniel Maier,[33,34] Kazuo Makishima,[58] Maxim Markevitch,[9]
Hironori Matsumoto,[41] Kyoko Matsushita,[59] Dan McCammon,[60]
Brian R. McNamara,[61] Missagh Mehdipour,[4] Eric D. Miller,[15,†]
Jon M. Miller,[62] Shin Mineshige,[23] Kazuhisa Mitsuda,[22]
Ikuyuki Mitsuishi,[40] Takuya Miyazawa,[63] Tsunefumi Mizuno,[28,64]
Hideyuki Mori,[9] Koji Mori,[39] Koji Mukai,[9,38] Hiroshi Murakami,[65]
Richard F. Mushotzky,[56] Takao Nakagawa,[22] Hiroshi Nakajima,[41]
Takeshi Nakamori,[66] Shinya Nakashima,[58] Kazuhiro Nakazawa,[13,14]
Kumiko K. Nobukawa,[67] Masayoshi Nobukawa,[68] Hirofumi Noda,[69,70]

Hirokazu ODAKA,[6] Takaya OHASHI,[25] Masanori OHNO,[28] Takashi OKAJIMA,[9]
Naomi OTA,[67] Masanobu OZAKI,[22] Frits PAERELS,[71] Stéphane PALTANI,[10]
Robert PETRE,[9] Ciro PINTO,[26] Frederick S. PORTER,[9] Katja POTTSCHMIDT,[9,38]
Christopher S. REYNOLDS,[56] Samar SAFI-HARB,[72] Shinya SAITO,[43]
Kazuhiro SAKAI,[9] Toru SASAKI,[59] Goro SATO,[22] Kosuke SATO,[59] Rie SATO,[22]
Toshiki SATO,[25] Makoto SAWADA,[73] Norbert SCHARTEL,[52]
Peter J. SERLEMTSOS,[9] Hiromi SETA,[25] Megumi SHIDATSU,[58]
Aurora SIMIONESCU,[22] Randall K. SMITH,[16] Yang SOONG,[9] Łukasz STAWARZ,[74]
Yasuharu SUGAWARA,[22] Satoshi SUGITA,[49] Andrew SZYMKOWIAK,[20]
Hiroyasu TAJIMA,[5] Hiromitsu TAKAHASHI,[28] Tadayuki TAKAHASHI,[22]
Shin'ichiro TAKEDA,[63] Yoh TAKEI,[22] Toru TAMAGAWA,[75] Takayuki TAMURA,[22]
Takaaki TANAKA,[51] Yasuo TANAKA,[76,22] Yasuyuki T. TANAKA,[28]
Makoto S. TASHIRO,[77] Yuzuru TAWARA,[40] Yukikatsu TERADA,[77]
Yuichi TERASHIMA,[11] Francesco TOMBESI,[9,38,78] Hiroshi TOMIDA,[22]
Yohko TSUBOI,[48] Masahiro TSUJIMOTO,[22] Hiroshi TSUNEMI,[41]
Takeshi Go TSURU,[51] Hiroyuki UCHIDA,[51] Hideki UCHIYAMA,[79]
Yasunobu UCHIYAMA,[43] Shutaro UEDA,[22] Yoshihiro UEDA,[23]
Shin'ichiro UNO,[80] C. Megan URRY,[20] Eugenio URSINO,[30] Shin WATANABE,[22]
Norbert WERNER,[28,81,82] Dan R. WILKINS,[6] Brian J. WILLIAMS,[57]
Shinya YAMADA,[25] Hiroya YAMAGUCHI,[9,56] Kazutaka YAMAOKA,[5,40]
Noriko Y. YAMASAKI,[22] Makoto YAMAUCHI,[39] Shigeo YAMAUCHI,[67]
Tahir YAQOOB,[9,38] Yoichi YATSU,[49] Daisuke YONETOKU,[27] Irina ZHURAVLEVA,[6,7]
and Abderahmen ZOGHBI[62]

[1] Dublin Institute for Advanced Studies, 31 Fitzwilliam Place, Dublin 2, Ireland
[2] Max-Planck-Institut für Kernphysik, P.O. Box 103980, 69029 Heidelberg, Germany
[3] Gran Sasso Science Institute, viale Francesco Crispi, 7 67100 L'Aquila (AQ), Italy
[4] SRON Netherlands Institute for Space Research, Sorbonnelaan 2, 3584 CA Utrecht, the Netherlands
[5] Institute for Space-Earth Environmental Research, Nagoya University, Furo-cho, Chikusa-ku, Nagoya, Aichi 464-8601, Japan
[6] Kavli Institute for Particle Astrophysics and Cosmology, Stanford University, 452 Lomita Mall, Stanford, CA 94305, USA
[7] Department of Physics, Stanford University, 382 Via Pueblo Mall, Stanford, CA 94305, USA
[8] SLAC National Accelerator Laboratory, 2575 Sand Hill Road, Menlo Park, CA 94025, USA
[9] NASA, Goddard Space Flight Center, 8800 Greenbelt Road, Greenbelt, MD 20771, USA
[10] Department of Astronomy, University of Geneva, ch. d'Écogia 16, CH-1290 Versoix, Switzerland
[11] Department of Physics, Ehime University, 2-5 Bunkyo-cho, Matsuyama, Ehime 790-8577, Japan
[12] Department of Physics and Oskar Klein Center, Stockholm University, 106 91 Stockholm, Sweden
[13] Department of Physics, The University of Tokyo, 7-3-1 Hongo, Bunkyo-ku, Tokyo 113-0033, Japan
[14] Research Center for the Early Universe, School of Science, The University of Tokyo, 7-3-1 Hongo, Bunkyo-ku, Tokyo 113-0033, Japan
[15] Kavli Institute for Astrophysics and Space Research, Massachusetts Institute of Technology, 77 Massachusetts Avenue, Cambridge, MA 02139, USA
[16] Smithsonian Astrophysical Observatory, 60 Garden St., MS-4., Cambridge, MA 02138, USA
[17] Lawrence Livermore National Laboratory, 7000 East Avenue, Livermore, CA 94550, USA
[18] Department of Physics and Astronomy, Wayne State University, 666 W. Hancock St, Detroit, MI 48201, USA
[19] Department of Astronomy, Yale University, New Haven, CT 06520-8101, USA

[20]Department of Physics, Yale University, New Haven, CT 06520-8120, USA

[21]Centre for Extragalactic Astronomy, Department of Physics, University of Durham, South Road, Durham DH1 3LE, UK

[22]Japan Aerospace Exploration Agency, Institute of Space and Astronautical Science, 3-1-1 Yoshino-dai, Chuo-ku, Sagamihara, Kanagawa 252-5210, Japan

[23]Department of Astronomy, Kyoto University, Kitashirakawa-Oiwake-cho, Sakyo-ku, Kyoto, Kyoto 606-8502, Japan

[24]The Hakubi Center for Advanced Research, Kyoto University, Yoshida-honmachi, Sakyo-ku, Kyoto, Kyoto 606-8501, Japan

[25]Department of Physics, Tokyo Metropolitan University, 1-1 Minami-Osawa, Hachioji, Tokyo 192-0397, Japan

[26]Institute of Astronomy, University of Cambridge, Madingley Road, Cambridge CB3 0HA, UK

[27]Faculty of Mathematics and Physics, Kanazawa University, Kakuma-machi, Kanazawa, Ishikawa 920-1192, Japan

[28]School of Science, Hiroshima University, 1-3-1 Kagamiyama, Higashi-Hiroshima, Hiroshima 739-8526, Japan

[29]Fujita Health University, 1-98 Dengakugakubo, Kutsukake-cho, Toyoake, Aichi 470-1192, Japan

[30]Physics Department, University of Miami, 1320 Campo Sano Dr., Coral Gables, FL 33146, USA

[31]Department of Astronomy and Physics, Saint Mary's University, 923 Robie Street, Halifax, NS, B3H 3C3, Canada

[32]Department of Physics and Astronomy, University of Southampton, Highfield, Southampton SO17 1BJ, UK

[33]Laboratoire APC, 10 rue Alice Domon et Léonie Duquet, 75013 Paris, France

[34]CEA Saclay, 91191 Gif sur Yvette, France

[35]European Space Research and Technology Center, Keplerlaan 1 2201 AZ Noordwijk, the Netherlands

[36]Department of Physics and Astronomy, Aichi University of Education, 1 Hirosawa, Igaya-cho, Kariya, Aichi 448-8543, Japan

[37]Department of Physics, Tokyo University of Science, 2641 Yamazaki, Noda, Chiba, 278-8510, Japan

[38]Department of Physics, University of Maryland Baltimore County, 1000 Hilltop Circle, Baltimore, MD 21250, USA

[39]Department of Applied Physics and Electronic Engineering, University of Miyazaki, 1-1 Gakuen Kibanadai-Nishi, Miyazaki, Miyazaki 889-2192, Japan

[40]Department of Physics, Nagoya University, Furo-cho, Chikusa-ku, Nagoya, Aichi 464-8602, Japan

[41]Department of Earth and Space Science, Osaka University, 1-1 Machikaneyama-cho, Toyonaka, Osaka 560-0043, Japan

[42]Department of Physics, Kwansei Gakuin University, 2-1 Gakuen, Sanda, Hyogo 669-1337, Japan

[43]Department of Physics, Rikkyo University, 3-34-1 Nishi-Ikebukuro, Toshima-ku, Tokyo 171-8501, Japan

[44]Department of Physics and Astronomy, Rutgers University, 136 Frelinghuysen Road, Piscataway, NJ 08854, USA

[45]Meisei University, 2-1-1 Hodokubo, Hino, Tokyo 191-8506, Japan

[46]Leiden Observatory, Leiden University, PO Box 9513, 2300 RA Leiden, the Netherlands

[47]Research Institute for Science and Engineering, Waseda University, 3-4-1 Ohkubo, Shinjuku, Tokyo 169-8555, Japan

[48]Department of Physics, Chuo University, 1-13-27 Kasuga, Bunkyo, Tokyo 112-8551, Japan

[49]Department of Physics, Tokyo Institute of Technology, 2-12-1 Ookayama, Meguro-ku, Tokyo 152-8550, Japan

[50]Department of Physics, Toho University, 2-2-1 Miyama, Funabashi, Chiba 274-8510, Japan

[51]Department of Physics, Kyoto University, Kitashirakawa-Oiwake-cho, Sakyo-ku, Kyoto, Kyoto 606-8502, Japan

[52]European Space Astronomy Center, Camino Bajo del Castillo, s/n., 28692 Villanueva de la Cañada, Madrid, Spain

[53] Universities Space Research Association, 7178 Columbia Gateway Drive, Columbia, MD 21046, USA

[54] National Science Foundation, 4201 Wilson Blvd., Arlington, VA 22230, USA

[55] Department of Electronic Information Systems, Shibaura Institute of Technology, 307 Fukasaku, Minuma-ku, Saitama, Saitama 337-8570

[56] Department of Astronomy, University of Maryland, College Park, MD 20742, USA

[57] Space Telescope Science Institute, 3700 San Martin Drive, Baltimore, MD 21218, USA

[58] Institute of Physical and Chemical Research, 2-1 Hirosawa, Wako, Saitama 351-0198, Japan

[59] Department of Physics, Tokyo University of Science, 1-3 Kagurazaka, Shinjuku-ku, Tokyo 162-8601, Japan

[60] Department of Physics, University of Wisconsin, Madison, WI 53706, USA

[61] Department of Physics and Astronomy, University of Waterloo, 200 University Avenue West, Waterloo, Ontario, N2L 3G1, Canada

[62] Department of Astronomy, University of Michigan, 1085 South University Avenue, Ann Arbor, MI 48109, USA

[63] Okinawa Institute of Science and Technology Graduate University, 1919-1 Tancha, Onna-son, Kunigami-gun, Okinawa 904-0495, Japan

[64] Hiroshima Astrophysical Science Center, Hiroshima University, 1-3-1 Kagamiyama, Higashi-Hiroshima, Hiroshima 739-8526, Japan

[65] Faculty of Liberal Arts, Tohoku Gakuin University, 2-1-1 Tenjinzawa, Izumi-ku, Sendai, Miyagi 981-3193, Japan

[66] Faculty of Science, Yamagata University, 1-4-12 Kojirakawa-machi, Yamagata, Yamagata 990-8560, Japan

[67] Department of Physics, Nara Women's University, Kitauoyanishi-machi, Nara, Nara 630-8506, Japan

[68] Department of Teacher Training and School Education, Nara University of Education, Takabatake-cho, Nara, Nara 630-8528, Japan

[69] Frontier Research Institute for Interdisciplinary Sciences, Tohoku University, 6-3 Aramakiazaaoba, Aoba-ku, Sendai, Miyagi 980-8578, Japan

[70] Astronomical Institute, Tohoku University, 6-3 Aramakiazaaoba, Aoba-ku, Sendai, Miyagi 980-8578, Japan

[71] Astrophysics Laboratory, Columbia University, 550 West 120th Street, New York, NY 10027, USA

[72] Department of Physics and Astronomy, University of Manitoba, Winnipeg, MB R3T 2N2, Canada

[73] Department of Physics and Mathematics, Aoyama Gakuin University, 5-10-1 Fuchinobe, Chuo-ku, Sagamihara, Kanagawa 252-5258, Japan

[74] Astronomical Observatory of Jagiellonian University, ul. Orla 171, 30-244 Kraków, Poland

[75] RIKEN Nishina Center, 2-1 Hirosawa, Wako, Saitama 351-0198, Japan

[76] Max-Planck-Institut für extraterrestrische Physik, Giessenbachstrasse 1, 85748 Garching, Germany

[77] Department of Physics, Saitama University, 255 Shimo-Okubo, Sakura-ku, Saitama, Saitama 338-8570, Japan

[78] Department of Physics, University of Rome "Tor Vergata", Via della Ricerca Scientifica 1, I-00133 Rome, Italy

[79] Faculty of Education, Shizuoka University, 836 Ohya, Suruga-ku, Shizuoka, Shizuoka 422-8529, Japan

[80] Faculty of Health Sciences, Nihon Fukushi University, 26-2 Higashi Haemi-cho, Handa, Aichi 475-0012, Japan

[81] MTA-Eötvös University Lendület Hot Universe Research Group, Pázmány Péter sétány 1/A, Budapest, 1117, Hungary

[82] Department of Theoretical Physics and Astrophysics, Faculty of Science, Masaryk University, Kotlářská 2, Brno, 611 37, Czech Republic

*Corresponding authors: Eric D. Miller, Hiroya Yamaguchi, Kumiko Nobukawa, Makoto Sawada, Masayoshi Nobukawa, Satoru Katsuda, and Hideyuki Mori.

†E-mail: milleric@mit.edu

Abstract

We present Hitomi observations of N 132 D, a young, X-ray bright, O-rich core-collapse supernova remnant in the Large Magellanic Cloud (LMC). Despite a very short observation of only 3.7 ks, the Soft X-ray Spectrometer (SXS) easily detects the line complexes of highly ionized S K and Fe K with 16–17 counts in each. The Fe feature is measured for the first time at high spectral resolution. Based on the plausible assumption that the Fe K emission is dominated by He-like ions, we find that the material responsible for this Fe emission is highly redshifted at $\sim 800\,\mathrm{km\,s^{-1}}$ compared to the local LMC interstellar medium (ISM), with a 90% credible interval of 50–1500 $\mathrm{km\,s^{-1}}$ if a weakly informative prior is placed on possible line broadening. This indicates (1) that the Fe emission arises from the supernova ejecta, and (2) that these ejecta are highly asymmetric, since no blueshifted component is found. The S K velocity is consistent with the local LMC ISM, and is likely from swept-up ISM material. These results are consistent with spatial mapping that shows the He-like Fe concentrated in the interior of the remnant and the S tracing the outer shell. The results also show that even with a very small number of counts, direct velocity measurements from Doppler-shifted lines detected in extended objects like supernova remnants are now possible. Thanks to the very low SXS background of ~ 1 event per spectral resolution element per 100 ks, such results are obtainable during short pointed or slew observations with similar instruments. This highlights the power of high-spectral-resolution imaging observations, and demonstrates the new window that has been opened with Hitomi and will be greatly widened with future missions such as the X-ray Astronomy Recovery Mission (XARM) and Athena.

Key words: ISM: individual objects (N 132 D) — ISM: supernova remnants — instrumentation: spectrographs — methods: observational — X-rays: individual (N 132 D)

1 Introduction

As the main drivers for matter and energy in the Universe, supernova remnants (SNRs) are excellent laboratories for studying nucleosynthesis yields and for probing the supernova (SN) engine and dynamics. Core-collapse SNRs, in particular, address fundamental questions related to the debated explosion mechanism and the aftermath of exploding a massive star.

The mechanism of core-collapse supernova explosions has been one of the central mysteries in stellar astrophysics. While one-dimensional simulations have failed to explode a star, only very recently successful explosions of massive stars have been achieved in three-dimensional simulations invoking convection or standing accretion shock instabilities (SASI; see Janka et al. 2016 for a recent review). The ejecta composition and dynamics as a function of the progenitor star's mass and environment have formed another puzzle, with predictions largely relying on the assumption of spherically symmetric models and with yields that vary depending on metallicity, mass loss, explosion energy, and other assumptions (e.g., Nomoto et al. 2006; Woosley & Heger 2007).

Significant progress has been made to answer these central questions, thanks to high-resolution imaging and spectroscopic mapping of ejecta (in space and velocity) in core-collapse SNRs, including the oxygen-rich, very young and bright Cassiopeia A SNR in our Galaxy (Hwang & Laming 2012; Grefenstette et al. 2014) and more evolved SNRs with ejecta signatures such as the O-rich Galactic SNRs G292.2+1.8 (Park et al. 2007; Kamitsukasa et al. 2014) and Puppis A (Hwang et al. 2008; Katsuda et al. 2013), and the ejecta-dominated SNR W 49 B (Lopez et al. 2013a, 2013b). While such observations have opened a new window to understanding the physics and aftermath of core-collapse explosions, several complications remain in interpreting the observations. First, resolving ejecta from the shocked interstellar medium (ISM) requires fine spectral resolution of extended objects in the X-ray. Secondly, there is a strong dependence of the elemental distribution and plasma state on both the evolutionary stage of the SNR and on the surrounding environment shaped by the exploded progenitor star. Mixed-morphology SNRs, expanding into an inhomogeneous medium and often interacting with molecular clouds, need the additional treatment of over-ionized (recombining) plasma, as opposed to under-ionized (ionizing) plasma in the younger remnants or SNRs expanding into a low-density and homogeneous medium (e.g., Ozawa et al. 2009; Uchida et al. 2015).

The advent of high-spectral-resolution imaging detectors such as the Soft X-ray Spectrometer (SXS) aboard Hitomi has promised to revolutionize our three-dimensional mapping of ejecta dynamics and composition, while spectroscopically differentiating between shocked ejecta and the shocked circumstellar/interstellar environment shaped by the progenitor star (Takahashi et al. 2016; Hughes et al. 2014).

A natural early target for Hitomi was N 132 D, the X-ray brightest SNR in the LMC, with an age estimated to be ∼ 2500 yr (Vogt & Dopita 2011). High-velocity ejecta were first detected and studied in optical wavelengths in N 132 D (Danziger & Dennefeld 1976; Sutherland & Dopita 1995; Morse et al. 1995, 1996). Optical/UV spectra from the Hubble Space Telescope show strong emission of C/Ne-burning elements (i.e., C, O, Ne, Mg), but little emission from O-burning elements (i.e., Si, S), leading to an interpretation of a Type Ib core-collapse supernova origin for this SNR (Blair et al. 2000).

In the X-ray band, the Einstein Observatory made the first observation of N 132 D, revealing its clear shell-like morphology (Mathewson et al. 1983) which has been interpreted as arising from the SN blast wave expanding within a cavity produced by the progenitor star's H II region (Hughes 1987). Einstein also performed the first high-resolution spectral observations with the Focal Plane Crystal Spectrometer (FPCS), clearly seeing strong oxygen and other emission lines and obtaining the first measurements of line flux ratios and constraints on the temperature and ionization state (Hwang et al. 1993). The following ASCA observations revealed that elemental abundances of the entire SNR are consistent with the mean LMC values. This suggests that the X-ray-emitting plasma is dominated by the swept-up ISM (Hughes et al. 1998). Beppo-SAX detected Fe K line emission arising from a hot plasma (Favata et al. 1997). High-resolution X-ray images from XMM-Newton and Chandra have shown that the Fe K-emitting material is concentrated in the interior of the SNR, contrasting with the material emitting at softer energies of O, Ne, Mg, Si, S, and Fe L (Behar et al. 2001; Canizares et al. 2001; Borkowski et al. 2007; Xiao & Chen 2008; Plucinsky et al. 2016). X-ray emission from O-rich ejecta knots has also been discovered with Chandra, showing a spatial correlation with the optical O emission (Borkowski et al. 2007). The centroid and intensity of the Fe K line emission measured with Suzaku support the core-collapse origin (Yamaguchi et al. 2014). Very recently, a combined NuSTAR and Suzaku analysis revealed that the hot, Fe K-emitting plasma is in a recombining state with a large relaxation timescale of ∼ 10^{12} cm^{-3} s, implying that the plasma underwent rapid cooling in the very beginning of its life (Bamba et al. 2018).

N 132 D is the brightest among all known SNRs in GeV and TeV bands (Ackermann et al. 2016; H.E.S.S. Collaboration 2015). The spectral energy distribution from radio to gamma-rays including synchrotron X-rays detected with NuSTAR suggests that the gamma-ray emission originates from hadronic processes (Bamba et al. 2018). The total proton energy required to explain the spectral energy distribution was derived to be ∼ 10^{50} erg, showing that N 132 D is an efficient particle accelerator.

We here present Hitomi observations of N 132 D. These commissioning phase observations were expected to explore the emission line structure of the remnant with exquisite spectral resolution, unprecedented for an extended object at the energy of Fe K (∼ 6.7 keV). Unfortunately, due to poor satellite attitude control during the majority of the observation (see section 2 for details), only a short exposure was obtained with the Hitomi/SXS microcalorimeter. Nevertheless, owing to the excellent spectral resolution and gain accuracy of the SXS, we detect spectral features of strong emission from S, Ar, and Fe, allowing us to investigate the bulk velocity of the shocked material in this SNR using the Doppler shift of these emission lines. We demonstrate the superior capability of high-resolution spectrometers particularly for low-statistics data, which provide positive prospects for future observations of distant or faint objects with future X-ray microcalorimeter missions, like the X-ray Astronomy Recovery Mission (XARM), Athena (Nandra et al. 2013), and Lynx.[1] We also present the analysis of Soft X-ray Imager (SXI) data, simultaneously obtained from this observation but with longer exposure (and hence higher statistics) owing to its wide field of view (FoV).

This paper is organized as follows. In section 2, we describe the details of the Hitomi observations. We present spectral analysis of the SXS and SXI in sections 3 and 4, respectively. We discuss the results in section 5 and summarize in section 6. Throughout the paper, we assume 50 kpc for the distance to the LMC (Westerlund 1990), and $v_{\mathrm{helio,\,LMC}} = 275 \pm 4$ km s^{-1} as the heliocentric velocity of the LMC ISM immediately surrounding N 132 D (Vogt & Dopita 2011). Heliocentric velocities noted by v_{helio} have been corrected to the solar system barycentric standard of rest. The errors quoted in the text and table represent the 90% confidence level, and the error bars given in the spectra represent 68% confidence.

2 Observations and data reduction

The Hitomi X-ray Observatory was launched in 2016 February and tragically lost at the end of March of that year
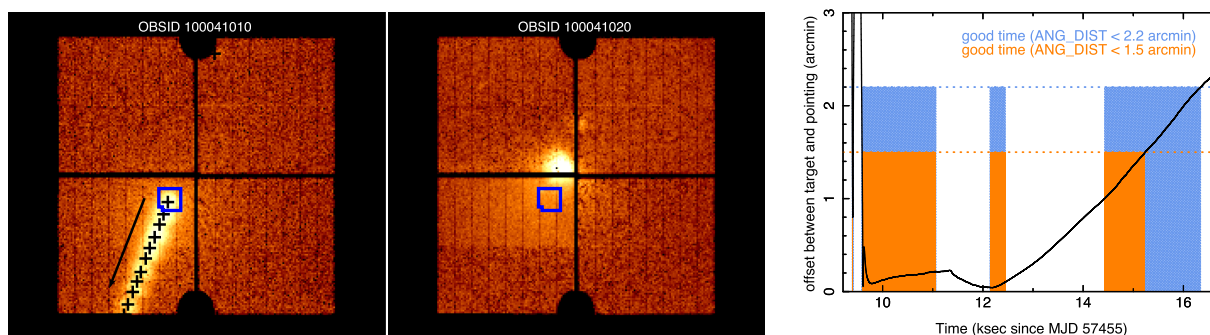
---

[1] ⟨https://wwwastro.msfc.nasa.gov/lynx⟩.

Fig. 1. Left: SXI images in detector coordinates showing the two OBSIDs used in the SXI analysis. The blue square shows the SXS FoV. The arrow in the left-hand panel shows the direction N 132 D drifted in the focal plane during that OBSID, with black crosses marking the source center in intervals of one hour. N 132 D was in the SXS FoV for only 3.7 ks of OBSID 100041010, and for none of OBSID 100041020. The remnant was still visible in SXI due to that detector's larger FoV. Right: Attitude of Hitomi during the first 7 ks of OBSID 100041010. The solid line shows `ANG_DIST`, the angular distance in arcminutes between the intended pointing and the actual pointing. Bins show the good time intervals of the default data filtering, which requires `ANG_DIST` < 1'.5, and the additional ∼43% of time added by relaxing this criterion to 2'.2. Blank times are excluded because of Earth's occultation or the South Atlantic Anomaly passage. (Color online)

(Takahashi et al. 2016). During the month of operation, the SXS successfully demonstrated its in-orbit performance by achieving an unprecedented spectral resolution ($\Delta E \approx$ 5 eV) across a broad energy (2–12 keV) for extended sources (Kelley et al. 2016; Porter et al. 2016a). This led to accurate determination of the turbulent velocity of hot plasma in the Perseus Cluster by measuring the line width of the Fe XXV Heα fine structure (Hitomi Collaboration 2016).

After the Perseus observations, Hitomi aimed at the SNR N 132 D for performance verification of the SXS and SXI using another line-rich source. The other detectors, the Hard X-ray Imager (HXI) and Soft Gamma-ray Detector (SGD), were not yet turned on. Unfortunately, the satellite attitude control system lost control about 30 minutes after the observation started due to problems in the star tracker system, as illustrated in figure 1. Because of this, the SNR drifted out of the 3′ × 3′ SXS FoV and remained out of view for the remainder of the observation. Thanks to its larger FoV, the SXI was able to observe the source during the entire observation.

As this observation took place during the commissioning phase, several instrument settings were non-standard compared to expected science operation. First, the SXS gate valve was in the closed configuration to reduce the chance of molecular contamination from spacecraft out-gassing. The gate valve had a ∼ 260 μm thick Be window to allow observations while closed, but this absorbed almost all X-rays below ∼ 2 keV and reduced the effective area by ∼ 50% at higher energies (Eckart et al. 2016). Thus we limit our SXS analysis to the 2–10 keV regime. Secondly, while the SXS was close to thermal equilibrium at this point in the commissioning phase (Fujimoto et al. 2016; Noda et al. 2016), no on-orbit, full-array energy scale (or gain) calibration had been performed with the filter-wheel calibration sources. The Modulated X-ray Source (MXS: de Vries et al. 2018)

was also not available for contemporaneous gain measurement. A dedicated calibration pixel that was outside of the aperture and continuously illuminated by a collimated ^{55}Fe source served as the only contemporaneous energy-scale reference, and the time-dependent scaling required to correct its gain was applied to each pixel in the array (Porter et al. 2016b). It was well known prior to launch that the time-dependent gain-correction function for this calibration pixel generally would not adequately correct the energy scale of the array pixels. In particular, the relationship between changes on the calibration pixel and on the array was not fixed, but rather depended on the temperatures of various shields and interfaces in the SXS dewar. Therefore, although the relative drift rates across the array were characterized during a later calibration with the filter-wheel ^{55}Fe source (M. E. Eckart et al. in preparation), changes in SXS cryocooler settings between the N 132 D observation and that calibration limit the usefulness of that characterization.

In fact, the measured relative gain drift predicts a much larger energy-scale offset between the final two pointings of the Perseus Cluster than was actually observed. Using source-free SXS observations taken during the period with the same cryocooler settings as the N 132 D observation (2016 March 7–15) in order to circumvent this limitation, we measured the center of the Mn Kα instrumental line (Kilbourne et al. 2018), and conclude that the SXS energy scale is shifted by at most $+1 \pm 0.5$ eV at 5.9 keV (M. E. Eckart et al. in preparation). There are no sufficiently strong low-energy lines in the same data set, but extrapolating from Perseus Cluster observations, we estimate a gain shift of -2 ± 1 eV at 2 keV (Hitomi Collaboration 2018). In the filter-wheel ^{55}Fe data set, errors in the position of the Mn Kβ line ranged from -0.6 to $+0.2$ eV across the array. Since this line is at 6.5 keV, less than 1 keV from the Mn Kα reference line, gain errors at other energies further from
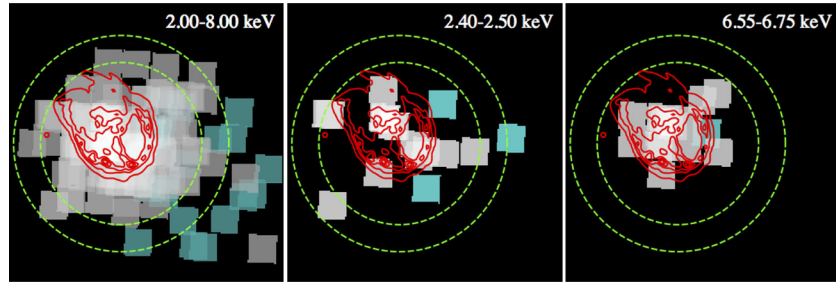
Fig. 2. Images of the SXS showing individual counts as a pixels on the sky. Blue boxes are counts included after relaxing the angular distance criterion. The red contours trace the Chandra emission, and the green circles show radii of 1.′5 and 2.′0 from the Chandra peak. The counts in Fe K (right) correspond well to the remnant extent, while some of the counts in the other bands are outside the bounds of the remnant.

the reference may be substantial. This is especially true in science data, for which any drift of the energy scale can only be corrected via the data from the calibration pixel. To be conservative, we use a systematic gain error of ± 2 eV at all energies in the analysis below.

We analyzed the cleaned event data of the final pipeline processing (Hitomi software version 6, CALDB version 7) with the standard screening for both SXS and SXI (Angelini et al. 2016), with one exception. To maximize the good SXS observing time, we relaxed the requirement that eliminates data when the aimpoint is further than 1.′5 from the target position. Using a maximum angular offset of 2.′2 ensures that at least 50% of the SNR is still in the FoV, and it increases the good SXS exposure time from 2610 s to 3737 s (by 43%) and the total SXS counts in the 2–10 keV band from 198 to 233 (by 18%). Relaxing this criterion increased the counts in the Fe XXV Heα band (defined in subsection 3.1) from 16 to 17, and in the S XV Heα band (defined in subsection 3.2) from 13 to 16. As we show in section 3, with the very low SXS background and very high spectral resolution, this small number of counts is sufficient to derive interesting constraints for the line centers. Some of the additional broad-band counts are from the region outside the N 132 D emission peak, as shown in figure 2, so they are likely background counts. The extra counts in the lines are consistent with locations in the remnant, also shown in figure 2; in particular, to the extent that we can infer locations from the $\sim 1'$ Hitomi PSF, the S counts are found largely in the rim of the remnant, while all the Fe K counts are concentrated in the remnant center, consistent with what is seen with XMM-Newton (Behar et al. 2001).

We constructed an SXS source spectrum by extracting only GRADE Hp (high-resolution primary) events from the entire SXS field of view of OBSID 100041010, and created the redistribution matrix file (RMF) with `sxsrmf`, using the medium size option. The ancillary response file (ARF) was generated with `aharfgen`, using a high-resolution Chandra image as input to the ray-tracing. A non-X-ray background (NXB) spectrum with the same sampling of magnetic

cut-off rigidity as the observation and with identical filtering as the source data (except for Earth elevation criteria) was extracted from the SXS archive NXB event file using `sxsnxbgen`. In the 2–10 keV band, we expect 23.2 ± 0.6 NXB counts, about 10% of the observed count rate, and corresponding to ~ 0.4 counts per spectral resolution element per 100 ks. In the narrow bands used for the analysis that follows, the NXB count rate is less than 5% of the observed rate as the SXS NXB is almost featureless and nearly constant over the energy range (M. E. Eckart et al. in preparation).

For the SXI, both OBSIDs 100041010 and 100041020 were used, although for the former we enforced the requirement that the aimpoint be within 1.′5 of the target to eliminate complications in constructing a response for a source moving across the FoV. For OBSID 100041020, we used only times when the attitude was stable, although the source was not at the expected aimpoint and was partially obstructed by the chip gaps (see figure 1). The final good exposure time for the SXI was 35.4 ks.

An SXI spectrum was extracted from a 2.′5 radius circle with center (RA, Dec) = ($5^h 25^m 02.^s 2$, $-69°38'39''$). The NXB spectrum was produced with `sxinxbgen`, using the entire SXI FoV excluding the source in order to increase the statistics. To properly scale the NXB normalization between the full FoV and source region, the instrumental lines of Au Lα and Lβ were used, producing a scaling factor of 0.0070. RMF and ARF files were generated with and `sxirmf` and `aharfgen`, respectively.

3 SXS spectral analysis

With only 233 counts, the SXS spectrum is dominated by Poisson low-count statistics. In addition, with the SXS gate valve closed, the bright emission lines of C, O, Ne, and Mg below 2 keV are not observable. However, three emission features are easily seen in the full-band spectrum shown in figure 3: the Heα transition features of He-like S (~ 2.45 keV), Ar (~ 3.1 keV), and Fe (~ 6.7 keV).
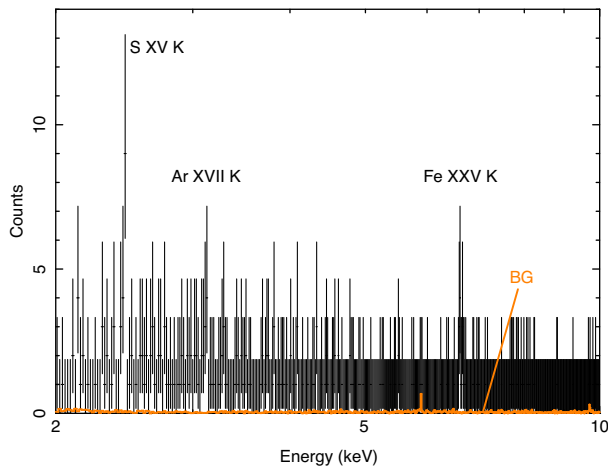
Fig. 3. Full-band SXS spectrum of N 132 D, showing counts with Poisson errorbars from Gehrels (1986). The points labeled "BG" show the total estimated background, which has not been subtracted. Both spectra are binned to 16 eV for display purposes. (Color online)

These lines are clearly detected in previous observations dating back to BeppoSAX (Favata et al. 1997), although the combination of an extended source and lower sensitivity at these energies complicates their measurement by X-ray grating instruments like Chandra/HETGS and XMM-Newton/RGS. From narrow bands centered on each expected line centroid, the total number of counts and estimated NXB counts are 16 total (0.30 ± 0.07 NXB) counts for S XV Heα, 14 total (0.28 ± 0.06 NXB) counts for Ar XVII Heα, and 17 total (0.8 ± 0.1 NXB) counts for Fe XXV Heα. The signal-to-noise ratio of these features and the underlying continuum is insufficient to obtain useful constraints on the metal abundance, temperature, or velocity broadening of the emitting plasma. However, as we show below, given a reasonable spectral model from other sources, the exquisite spectral resolution of SXS allows us to measure the line centers and thus the average line-of-sight Doppler velocity of two of these components, S and Fe.

All spectral fitting described below was performed with XSPEC v12.9.1d (Arnaud 1996), using atomic and non-equilibrium ionization (NEI) emissivity data from AtomDB v3.0.8 (Foster et al. 2012), and abundance ratios from Anders and Grevesse (1989). In each restricted fitting region, we allowed only the line-of-sight velocity and normalization of the appropriate thermal component (described below) to vary in the initial fit. While we include the cosmic X-ray background (CXB), it is negligible; a reasonable model for the 2–10 keV contribution of the CXB power-law component with $\Gamma = 1.4$, $S(2\text{--}10\,\mathrm{keV}) = 5.4 \times 10^{-15}\,\mathrm{erg\,cm^{-2}\,s^{-1}\,arcmin^{-2}}$ (e.g., Ueda et al. 1999; Bautz et al. 2009) predicts a mean of 1.5 CXB counts across the entire band and fewer than 0.1 CXB counts in any of the narrow spectral analysis bands. This is less than 1% of the

detected counts. Galactic foreground emission is negligible above 2 keV toward this direction ($l = 280°$, $b = -32°.8$).

3.1 Iron region spectral analysis

Fe K emission in N 132 D has been explored previously (Favata et al. 1997; Behar et al. 2001; Xiao & Chen 2008; Yamaguchi et al. 2014), with the conclusion that this feature is dominated by Fe XXV Heα emission. The XMM-Newton/EPIC observations are successfully fitted above 2.5 keV with a two-temperature-component model with $kT = 0.89$ and 6.2 keV (Behar et al. 2001). The cooler component produces the strong soft emission lines seen with XMM-Newton/RGS, and the hotter component explains the Fe K emission. In particular, Behar et al. (2001) emphasize the lack of a temperature component at ~ 1.5 keV to explain the lack of observed L-shell emission from Li-, Be-, and B-like Fe in the XMM-Newton spectrum. A recent study using 240 ks of Suzaku data combined with a 60 ks NuSTAR observation (Bamba et al. 2018) has produced a two-component broad-band spectral model of N 132 D with a similar cool temperature ($kT \approx 0.8$ keV) but that interprets the Fe K emission arising primarily from an over-ionized, recombining plasma component with $kT_e = 1.5$ keV, $kT_{init} > 20$ keV, and relaxation timescale $n_e t \approx 10^{12}\,\mathrm{s\,cm^{-3}}$. Crucially, the Suzaku data show a clear detection of H-like Fe Lyα emission, indicating that an under-ionized (ionizing) plasma is unlikely to contribute significantly to the emission at these energies, and thus much of the otherwise unresolved Fe K emission is likely due to He-like Fe rather than lower ionization states.

These previous observations provide confidence that we know where the line centroid should be for the Fe K complex, and can cleanly measure the line-of-sight velocity. However, we emphasize that this is one possible interpretation of a plasma with strong Fe XXV Heα and measurable Fe XXVI Lyα emission. A more complicated temperature structure, such as from multiple unassociated, spatially unresolved components, could produce a very different complex of lines in this spectral region. We address this possibility further in section 5. To ease comparison to current work, we adopt the model from Bamba et al. (2017) as a baseline model, shown in figure 4 and table 1.

The Fe XXV Heα complex, shown in figure 5, was fitted within the energy range 6.45–6.80 keV. This range includes sufficient width to constrain the continuum and measure velocity shifts up to $\sim 7000\,\mathrm{km\,s^{-1}}$, but avoids contamination from a possible 6.4 keV Fe K line and any H-like Fe features. It is clear from figure 4 that in this very clean fitting region the model is dominated by emission from the recombining plasma component by at least a factor of 100 over
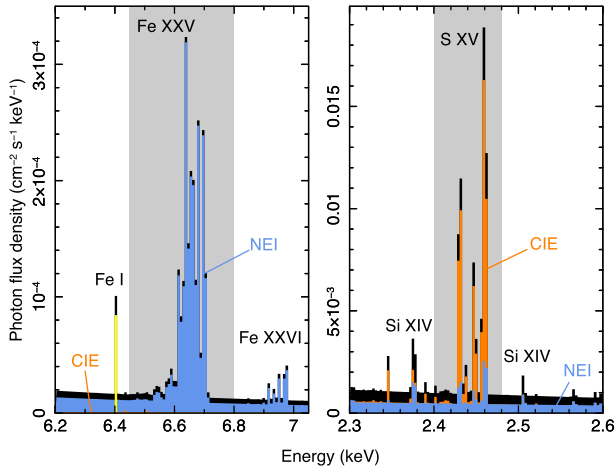
Fig. 4. N 132 D model spectrum, with contributions from individual components shown along with the total spectrum (black). All components are plotted with zero velocity and no line broadening. In the Fe XXV Heα band (left), the NEI component (blue) dominates by a factor of ∼ 100 over the component (orange). In the S XV Heα band (right), the CIE component is ∼ 10 times brighter than all other components. The gray shading indicates the bands used for spectral analysis; the S region is chosen to exclude contributions from Si XIV, while the Fe region is chosen to exclude the bright neutral line (yellow) and the Fe XXVI feature, but include possible contributions from lower ionization states of Fe near 6.5 keV. (Color online)

the cooler collisional ionization equilibrium (CIE) component. Therefore, while we included the entire model with all components for the Fe region fit, we only allowed parameters related to the NEI component to vary. To allow for differences in the observed flux due to the smaller SXS FoV and attitude drift, we fixed the ratio of the CIE to NEI component normalizations to that derived by Bamba et al. (2017), and allowed the NEI flux to vary along with the line-of-sight velocity. The CIE component was modeled by a variable-abundance `vapec` model in XSPEC, while the NEI component was modeled by a variable-abundance recombining plasma model, `vrnei`. We included a single Gaussian broadening parameter to allow for thermal and turbulent broadening as well as unresolved bulk motion.

Parameter estimation was performed in two ways. First, maximum likelihood estimation was done by minimizing the fit statistic, using `cstat` in XSPEC, a modified Cash (1979) statistic. With the broadening width fixed at zero, this fitting revealed a highly non-monotonic parameter space for the velocity (see figure 6), likely due to the combination of low-count Poisson statistics in the data and discrete spectral features in the model. The best-fitting velocity of $v_{helio} = 1440 \, km \, s^{-1}$ is significantly larger than the value of the local LMC ISM surrounding N 132 D, $v_{helio, LMC} = 275 \pm 4 \, km \, s^{-1}$ (Vogt & Dopita 2011). Allowing a free broadening width eliminated this non-monotonicity (see figure 7), resulting in a best-fitting $v_{helio} = 1140 \, km \, s^{-1}$ and broadening of $\sigma = 510 \, km \, s^{-1}$.

Secondly, to fully explore parameter space, we performed Markov chain Monte Carlo (MCMC) simulations within XSPEC using Bayesian inference. These simulations were run with and without velocity broadening, using both a flat (uniform) prior distribution and a Gaussian prior distribution for the broadening width. The width of the Gaussian prior distribution was chosen to reflect current upper limits on the velocity broadening. In particular, observations with CCD-based X-ray observatories such as Suzaku (e.g., Bamba et al. 2017) have not found measurable broadening. The typical spectral resolution of such instruments near 6 keV is ∼ 150–180 eV FWHM, depending on the epoch of observation, with a typical 1σ calibration uncertainty of 5%.[2] This calibration uncertainty can be thought of as an upper limit on the detectable line broadening velocity. Since the broadening is a convolution, this extra velocity component adds in quadrature with the instrumental width. We find that a 5% increase on the 150–180 eV FWHM instrumental width is equivalent to an extra broadening component with FWHM of 48–58 eV, or $\sigma = 900–1100 \, km \, s^{-1}$ in the center of our fitting band. We therefore adopted 1000 km s⁻¹ as a natural 1σ width to use for the Gaussian prior distribution. We performed MCMC simulations using both the flat, uninformative prior and the weakly informative Gaussian prior.

The MCMC results are consistent with the local `cstat` minima in velocity parameter space for fits with and without broadening, as shown by the MCMC posterior probability distributions in figures 6 and 7. In particular, the complicated velocity posterior distribution shows up clearly in the MCMC runs without broadening, but with the most likely value (highest mode) near $v_{helio} = 800 \, km \, s^{-1}$ instead of 1400 km s⁻¹ as found in the `cstat` minimization. The MCMC chain steps shown in figure 6 (right) indicate that the simulation is well-behaved and samples the posterior distribution adequately despite the multimodal structure. The runs with broadening result in Gaussian posterior distributions with peak near 1000 km s⁻¹. Using either a Gaussian or Cauchy form for the chain proposal distribution produced the same results.

We used these posterior distributions to obtain central credible intervals on v_{helio}. For the fit with no broadening, a single interval is uninformative due to the complicated structure. We obtain a 68% credible interval of 730–1460 km s⁻¹, 90% interval of 440–1540 km s⁻¹, and 95% interval of 160–1620 km s⁻¹. A line-of-sight velocity consistent with $v_{helio, LMC}$ is ruled out at 93% confidence under this model. With broadening, a single credible interval is sufficient to characterize the Gaussian-shaped distribution,

---

[2] See table 3.2 and figure 7.11 of the Suzaku Technical Description ⟨ftp://legacy.gsfc.nasa.gov/suzaku/nra_info/suzaku_td_xisfinal.pdf⟩.

Table 1. Results of SXS spectral fitting.*

Model parameter	Fe XXV fit		S XV fit	
	No broadening	With broadening[†]	No broadening	With broadening[†]
N 132 D CIE plasma (`vapec`)				
kT (keV)	.... 0.7			
Z_{Si} (solar)	.... 0.6			
Z_{S} (solar)	.... 0.9			
Z_{Fe} (solar)	.... 0.4			
v_{helio} (km s^{-1})	.... 0		210^{+370}_{-380}	520^{+770}_{-620}
σ (km s^{-1})	.... 0		0	520^{+780}_{-340}
Flux, 2–10 keV[‡]	.... 8.8		$5.6^{+2.9}_{-1.9}$	$5.5^{+3.1}_{-1.8}$
Flux, fitting band[‡]	.... 0.006		$1.3^{+0.4}_{-0.2}$	$1.3^{+0.4}_{-0.2}$
N 132 D NEI plasma (`vrnei`)				
kT (keV)	.... 1.5			
kT_{init} (keV)	.... 80			
$n_e t$ (10^{12} s cm^{-3})	.... 0.9			
Z_{Si} (solar)	.... 0.4			
Z_{S} (solar)	.... 0.4			
Z_{Fe} (solar)	.... 0.5			
v_{helio} (km s^{-1})	1440^{+100}_{-1000}	1140^{+640}_{-810}	1440	1140
σ (km s^{-1})	0	510^{+1060}_{-330}	0	510
Flux, 2–10 keV[‡]	$9.5^{+4.5}_{-3.0}$	$9.7^{+4.2}_{-3.2}$	6.1	6.2
Flux, fitting band[‡]	$0.48^{+0.25}_{-0.16}$	$0.49^{+0.24}_{-0.16}$	0.34	0.34
CXB power law				
Γ	.... 1.54			
Flux, 2–10 keV[‡]	.... 0.040			
Flux, fitting band[‡]	.... 0.0016		.... 0.0006	
Spectral fitting band	.... 6.45–6.80 keV		.... 2.40–2.48 keV	
C-stat/d.o.f.	107.9/696	106.5/695	61.0/157	59.1/156
Goodness-of-fit (KS)[§]	24%	20%	62%	31%
Goodness-of-fit (CvM)[§]	35%	21%	62%	46%

*Unless noted otherwise, values without quoted uncertainties are fixed. Uncertainties are 90% confidence limits.

[†]Results with broadening assume a Gaussian prior with $\sigma = 1000$ km s^{-1}.

[‡]Flux is given in units of 10^{-12} erg cm^{-2} s^{-1}. The ratio of the `vapec` and `vrnei` component normalizations was fixed to that in Bamba et al. (2017).

[§]"Goodness-of-fit" is the percentage of simulated observations with lower fit statistics than the real data, as described in subsection 3.1.
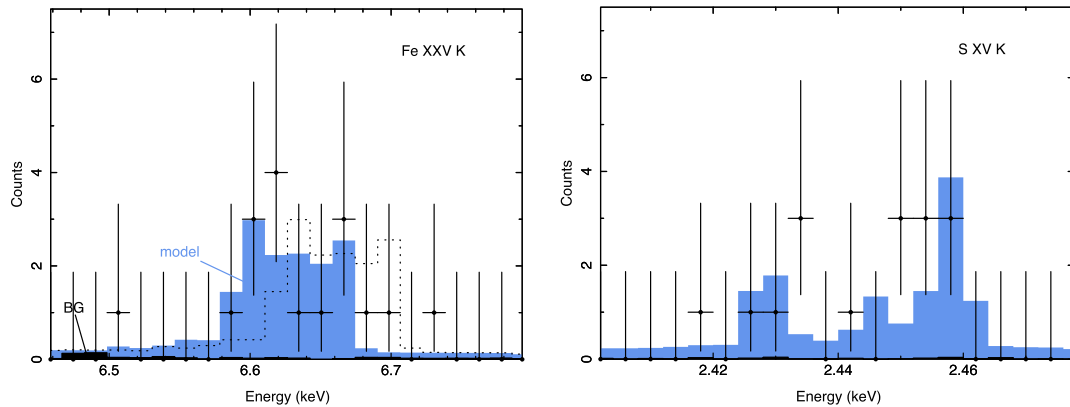
Fig. 5. SXS spectra of the (left) Fe XXV Heα and (right) S XV Heα fitting regions. The data points are detected SXS counts with Poisson error bars from Gehrels (1986). In both panels, the blue shaded region shows the best-fitting model, and the darker shaded region labeled "BG" barely visible, shows the estimated total background. In the left-hand panel, the dotted line shows the model with velocity fixed at $v_{helio, LMC} = 275$ km s^{-1}. The Fe spectrum is binned to 16 eV and S binned to 4 eV for display purposes. (Color online)
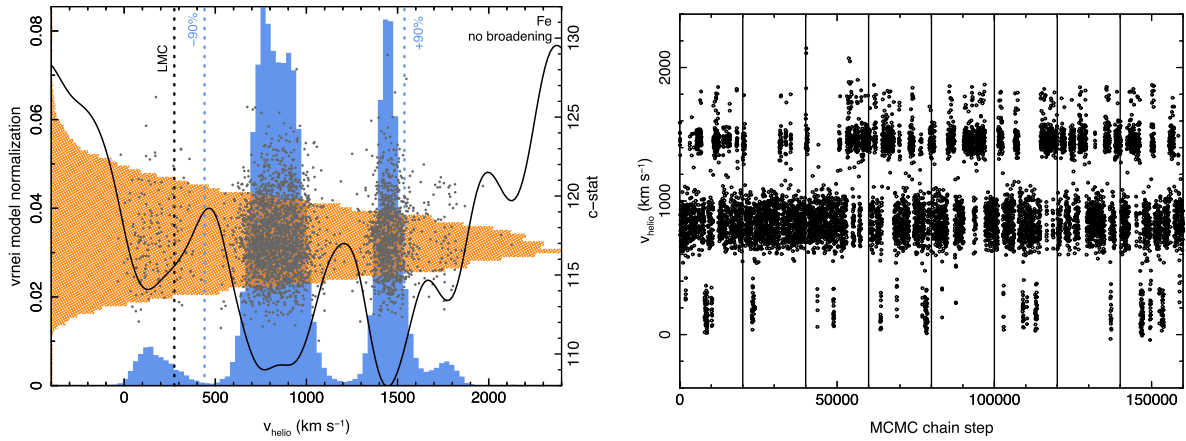
Fig. 6. Left: Posterior probability distributions of the `vrnei` model normalization (orange) and velocity (blue) from the Fe K region fitting without broadening, calculated from the MCMC analysis as described in the text. Points show sample MCMC chain steps, indicating that there is no correlation between the two parameters. The black line shows the `cstat` value from fit statistic minimization, as a function of best-fitting velocity. One peak of the MCMC velocity distribution coincides with the best-fitting velocity distribution, and other local peaks coincide with local `cstat` minima, indicating both maximum likelihood methods produce the same result. The dotted lines delineate the central 90% credible interval and note the local LMC velocity. Right: MCMC chain values for the Fe K velocity plotted against chain step, showing that the long-term variations of each chain are well-behaved and the posterior distribution is well-sampled. Vertical lines differentiate the eight individual 20000-step simulation chains. Steps within chains are in time order with one out of every ten steps shown for clarity. (Color online)
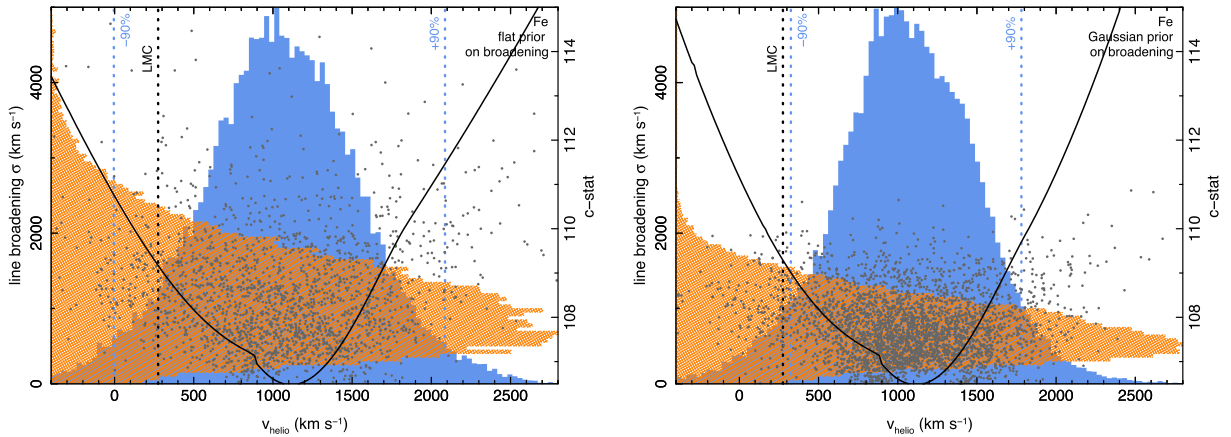
Fig. 7. Posterior probability distributions of the `vrnei` model broadening width and velocity from the Fe K region fitting including line broadening. Notations are the same as in figure 6. The left-hand panel shows results with flat prior on the line width, while the right-hand panel shows results imposing a Gaussian prior with 1σ width of $1000 \, \text{km s}^{-1}$. Both velocity distributions trace the `cstat` minimization well. The flat prior produces a broader posterior distribution. (Color online)

and we find 90% credible intervals of 330–$1780 \, \text{km s}^{-1}$ for broadening with a Gaussian prior distribution, and 0–$2090 \, \text{km s}^{-1}$ for a flat prior. The conservative gain uncertainty of $\pm 2 \, \text{eV}$ (see section 2) produces a systematic uncertainty of $\pm 90 \, \text{km s}^{-1}$, well within the statistical uncertainty. It is apparent that imposing an flat, uninformative prior on the broadening width distribution allows unrealistic values exceeding $\sigma = 3000 \, \text{km s}^{-1}$ with a broad tail to very high values. This greatly exceeds the thermal width of an Fe emission feature at $2 \, \text{keV}$ ($\sigma \sim 50 \, \text{km s}^{-1}$), and requires either extreme turbulence or very large bulk motions. If we adopt the results with the Gaussian prior, which has sufficient width to allow a blueshifted and redshifted

component separated by up to $\sim 2000 \, \text{km s}^{-1}$, a mean line-of-sight velocity consistent with $v_{\text{helio, LMC}}$ is ruled out at 91% confidence under this model. The model parameters are listed in table 1.

The measured photon flux in the fitting band, $4.6^{+2.3}_{-1.4} \times 10^{-5}$ photons cm^{-2} s^{-1}, is more than a factor of two higher than previous estimates of the Fe Kα line flux, e.g., $1.83 \pm 0.17 \times 10^{-5}$ photons cm^{-2} s^{-1} (Yamaguchi et al. 2014; errors are 90%). This is likely due to a combination of the Hitomi attitude uncertainty and the use of a broad-band X-ray image to produce the response files. While much of this broad-band X-ray emission is found in a shell with diameter $\sim 2'$, the Fe Kα emission appears centrally
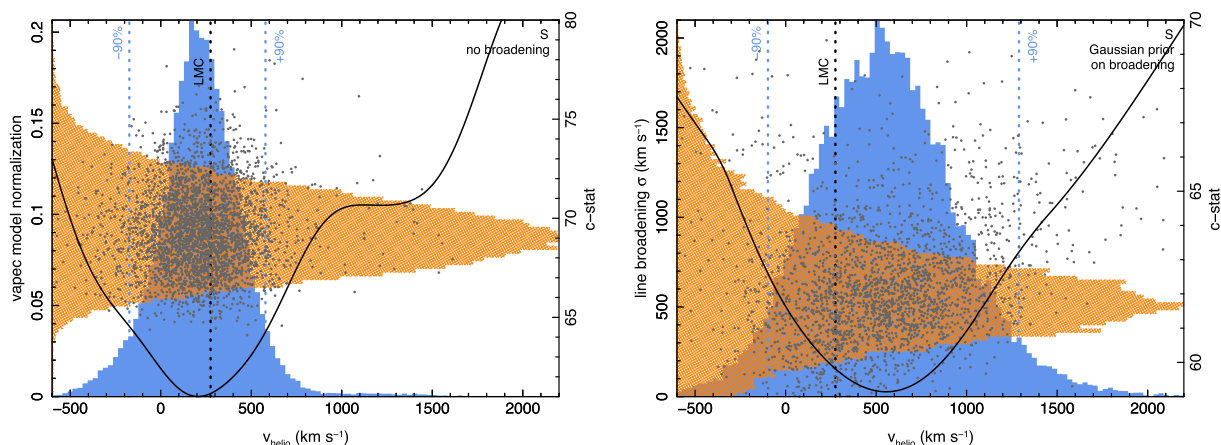
Fig. 8. Posterior probability distributions for the S region fit. In the left-hand panel, `vapec` model broadening is fixed at zero, and the posterior model normalization is shown on the Y axis. In the right-hand panel, a Gaussian prior with width $\sigma = 1000\,\mathrm{km\,s^{-1}}$ is imposed on the broadening, and the posterior broadening distribution is shown on the Y axis. The velocity posterior distribution is shown on the X axis in both panels. Other notations are the same as in figure 6. Both velocity posterior distributions are Gaussian in shape and trace the `cstat` minimization well. The model with broadening produces a broader distribution shifted to higher velocity, but still consistent with the local LMC velocity. (Color online)

concentrated (e.g., Behar et al. 2001). Using the more spatially extended broad-band image produces a lower response as some of the PSF-broadened flux falls outside of the $3' \times 3'$ SXS FOV, thereby increasing the inferred model flux for a given count rate. Our inclusion of data with large pointing offset of up to $2.'2$ and the large attitude drift undoubtedly exacerbate this effect. For this reason, the flux calibration is so uncertain that a flat, uninformative prior is a good representation of our knowledge of the SXS effective area for this observation.

Once the minimum fit statistic and parameter distribution function were determined, we explored the effects of adjusting other `vrnei` parameters within a reasonable range of uncertainty. In addition, we ran fits testing plasma models with higher over-ionization (setting $n_e t$ to a small value), under-ionization (an ionizing plasma, setting $kT_{\rm init} < kT$), and collisional ionization equilibrium (CIE, setting $kT_{\rm init} = kT$). The fit statistic was consistent in all cases, indicating that we cannot distinguish between various ionization states with the Hitomi/SXS data alone. In all cases, neither the best-fitting velocity nor its posterior distribution from the MCMC analysis changed appreciably, indicating that our results are insensitive to the exact emission model used so long as it is not highly complex.

Neither the XSPEC `cstat` statistic nor the MCMC analysis provides an estimate of the goodness-of-fit. We used two tests available in XSPEC, Kolmogorov–Smirnov (KS) and Cramer–von Mises (CvM), both of which treat the observed and model spectra as empirical distribution functions and compute a statistical difference between the two. Drawing parameter values for velocity, normalization, and broadening width from the full posterior distributions, we performed 1000 simulations of the observed 3.7 ks

spectrum for the fits with and without broadening. These simulated spectra were then fitted with the model, and the resulting KS and CvM test statistics were compared with the values from the original fits. For the fit without broadening, 24% of the realizations produced a smaller KS statistic than the best fit, and 35% produced a smaller CvM statistic. For the fits with broadening, the fractions were 20% for KS and 21% for CvM. We can only say that our best-fitting models are not statistically inconsistent with the data.

Since this asymmetric velocity structure is unexpected, we constrained a potential blueshifted emission feature by adding a second `vrnei` component with identical model parameters. The velocity of the first component was fixed to the best-fitting value of $1140\,\mathrm{km\,s^{-1}}$, while that of the new component was fixed to $-590\,\mathrm{km\,s^{-1}}$, to force symmetry about $v_{\rm helio, LMC}$. The `vrnei` normalizations, initially equal, were allowed to vary independently. We find that a blueshifted feature is allowed at up to 30% of the flux of the redshifted component, with a similar fit statistic and goodness-of-fit measure. Varying the blueshift within a reasonable range did not improve the fit or change the upper limit to its flux. The best-fitting broadening width ($\sigma \sim 500\,\mathrm{km\,s^{-1}}$ or FWHM $\sim 1200\,\mathrm{km\,s^{-1}}$) allows some blueshifted component, but the emission-weighted mean velocity is not centered on the LMC velocity. We conclude that the bulk of the He-like-iron-bearing material is receding asymmetrically, at a velocity $\sim 800\,\mathrm{km\,s^{-1}}$ with respect to the swept-up ISM surrounding N 132 D.

3.2 Sulfur region spectral analysis

Spectral fitting of the S XV Heα line proceeded in a similar manner to the Fe K region. We restricted the energy range

to 2.40–2.48 keV, leaving 16 total counts of which 0.30 ± 0.07 ($\sim 2\%$) are estimated to be from the NXB. Consistent with other recent work, we interpret the S XV Heα emission to arise predominantly from a CIE plasma with $kT \sim 1$ keV (Behar et al. 2001; Borkowski et al. 2007; Xiao & Chen 2008). In our baseline model, the CIE component dominates the NEI emission by a factor of ~ 5–10 in this region. Thus we allowed some small contamination from the high-redshift NEI emission by freezing the velocity and broadening of the `vrnei` component to the best-fitting values, and fixed the ratio of the `vapec` to `vrnei` normalizations to that found by Bamba et al. (2017). Only the velocity and normalization of the CIE `vapec` component were allowed to vary in the initial fit, but as with the Fe fit, we included broadening with similar priors to explore the effect on the derived velocity. The S region spectrum and model are shown in figure 5, posterior probability distributions are shown in figure 8, and best-fitting parameters are given in table 1.

Using the `cstat` maximum likelihood estimator, we obtain a best-fitting line-of-sight velocity of $v_{\rm helio} = 210$ km s^{-1} with broadening fixed at zero. Allowing a single broadening component results in $v_{\rm helio} = 520$ km s^{-1} with $\sigma = 520$ km s^{-1}. As with the Fe fitting, the posterior distributions in figure 8 are considerably wider when broadening is included, with 90% credible intervals on $v_{\rm helio}$ of -170 to $+580$ km s^{-1} with no broadening and -100 to $+1290$ km s^{-1} with a Gaussian prior on broadening with $\sigma = 1000$ km s^{-1}. Unlike for Fe, the velocity of the S component is completely unconstrained with a flat broadening prior. Our adopted SXS gain uncertainty of ± 2 eV (245 km s^{-1}; see section 2) is again well within this statistical uncertainty, which itself is consistent with the local LMC velocity of 275 km s^{-1}.

We performed additional spectral fitting, allowing kT of the CIE component and kT, $kT_{\rm init}$, $n_e t$, and σ of the recombining plasma component to vary over a broad range as in the Fe region fitting described in the previous section. The best-fitting velocity and credible intervals did not change. We performed the same goodness-of-fit tests to the S region fits as the Fe region fits, finding that 30%–60% of the simulated datasets produced a smaller test statistic. The model is thus consistent with the data, and we conclude that the He-like-sulfur-bearing gas is consistent with being at rest relative to the local LMC ISM, if we assume that line broadening is small.

3.3 Argon region spectral analysis

Spectral fitting of the Ar XVII Heα line is complicated by both the low number of total counts (14) and the estimated contributions from both CIE and NEI components.
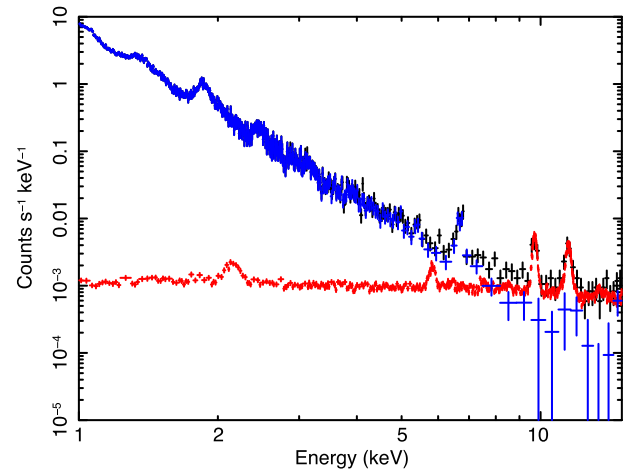
Fig. 9. SXI spectrum of N 132 D. Shown are the full spectrum, the scaled NXB spectrum, and the NXB-subtracted spectrum. Emission over the background is clearly seen above 10 keV. (Color online)

In fact, the Ar abundance is not constrained in either component, leading to a degeneracy between the normalization and abundance in each component and further difficulty fitting different velocities. As a simple test, we fixed the `vapec` and `vrnei` normalizations to the Bamba et al. (2017) values, fixed the Ar abundance to solar for both components, and fit a single line-of-sight velocity and normalization. The best-fitting velocity is $v_{\rm helio} = 2400$ km s^{-1}, with a 90% credible interval of 570–5900 km s^{-1}. This is consistent with both velocity ranges of Fe XXV and S XV. If the velocities are tied at the offset to the best-fitting values so that $v_{\rm vrnei} = v_{\rm vapec} + 1200$ km s^{-1}, the fit statistic is only slightly worse (`cstat` = 81.2 vs. 80.8), and the best-fitting values are $v_{\rm helio} = 1800$ km s^{-1} for the `vrnei` component and 600 km s^{-1} for the `vapec`, with similar uncertainties. Given the uncertainties in the model, we can only conclude that the Ar XVII fit is consistent with the Fe and S line results.

4 SXI spectral analysis

For the following analysis, the same version of XSPEC, AtomDB, NEI emissivity data, and abundance tables were used as in the analysis of the SXS spectrum (see section 3). The NXB-subtracted spectrum is shown in figure 9. In the N 132 D observation, the event and split thresholds are 600 eV and 30 eV, respectively. Since charge from a detected X-rays may be split among multiple CCD pixels, the quantum efficiency (QE) can be affected by split events well above the event threshold. Given the limited amount of calibration information available in these early observations, we conservatively exclude the energy band below 2 keV in this study.

We detect emission lines at 2.456 ± 0.010 keV and 6.68 ± 0.04 keV, which correspond to the same Heα lines of S and Fe detected in SXS, respectively. The SXI is affected by light leak when the satellite is in daylight, which can result in an observed line center shift (Nakajima et al. 2018). We investigated the line center shift in the N 132 D data, and confirmed that daylight illumination of the spacecraft has no effect. The S XV Heα line center is fully consistent with the centroid of the line complex measured with SXS (see figure 5). The Fe XXV Heα line center is marginally consistent with SXS within the uncertainty (see figure 5), and likely includes some unresolved contribution from Fe XXVI Lyα at ~ 7 keV (see figure 4).

Following the SXS analysis, we adopted a spectral model with two thin-thermal plasmas, a low-temperature `vapec` and high-temperature `vrnei`. From the model of Bamba et al. (2017), we also include a 6.4 keV neutral Fe K line, a non-thermal component, and the CXB. In the SXI analysis, the normalizations of the two plasmas are set to be free and all the other thermal parameters are fixed to those of Bamba et al. (2017). The normalization of the Fe I K line was tied to that of the `vrnei` component using the ratio of normalizations from Bamba et al. (2017). A power-law model was added for the possible non-thermal component, with both photon-index Γ and normalization allowed to vary. For the CXB, another power-law model with fixed parameters of $\Gamma = 1.4$ and surface brightness 5.4×10^{-15} erg cm^{-2} s^{-1} arcmin^{-2} in the 2–10 keV band was used (Ueda et al. 1999; Bautz et al. 2009). This CXB intensity is expected from observations with previous X-ray imaging instruments with similar PSF, and thus similar confusion limits. Since we are in the high-counts regime with at least 30 counts per spectral bin in the total (unsubtracted) source spectrum and high statistics in the NXB spectrum, we expect the background-subtracted spectral bins to be Gaussian distributed and use χ^2 minimization. We obtain $\chi^2/\mathrm{d.o.f.} = 234/243$ and an acceptable fit at the 90% confidence level. The best-fitting model with individual components is shown in figure 10. To check for potential bias in the use of χ^2 statistics, we perform the fit again excluding the poorest statistical region above 9 keV, and obtain similar results.

The lower and higher temperature plasmas produce the majority of the Heα lines of S and Fe, respectively, consistent with the result of the previous study (see also figure 4). The best-fitting `vapec` normalization was 0.92 ± 0.03 of the value from Bamba et al. (2017), while the `vrnei` was 0.86 ± 0.10 of their best-fitting value. The model fitting results in a non-thermal component with flux $1.3 \pm 1.1 \times 10^{-13}$ erg cm^{-2} s^{-1} in the 2–10 keV band. If we assume this non-thermal component exists, the fit constrains the photon index to be $\Gamma < 3.0$. With the SXI data
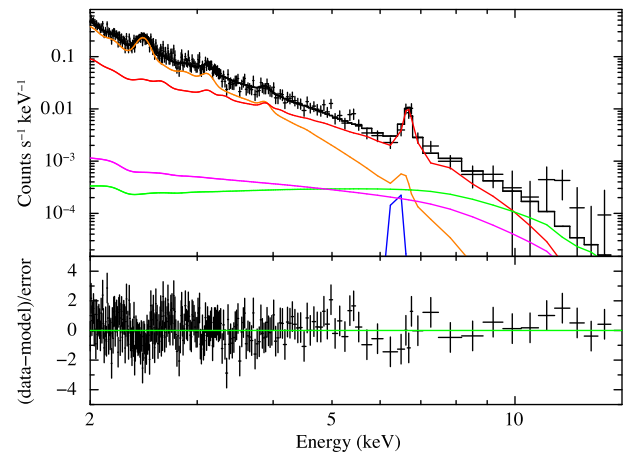
Fig. 10. SXI spectrum of N 132 D fitted with the model discussed in the text, with individual components shown. Two thin-thermal plasma components are shown with orange (`vapec`) and red (`vrnei`) lines. The 6.4 keV Fe K line is shown in blue, the CXB power law component in green, and the marginally detected non-thermal component in magenta.

in hand, we are unable to say conclusively that the non-thermal component is required, only that it is consistent with the observed spectrum.

5 Discussion

We have revealed a significant redshift of the emission lines of He-like Fe, constraining the line-of-sight velocity to be ~ 1100 km s^{-1}, or ~ 800 km s^{-1} faster than the local LMC ISM. The emission of S XV Heα, on the other hand, shows a velocity consistent with the radial velocity of the LMC ISM, albeit with large uncertainty, especially when broadening is included in the model. These results suggest different origins of the Fe and S emission: the former is dominated by the fast-moving ejecta and the latter by the swept-up ISM. This interpretation is consistent with the previous work by XMM-Newton, which revealed that the Fe emission has a centrally-filled morphology and the S emission is found along the outer shell (Behar et al. 2001).

This interpretation hinges on our assumed underlying emission model. Previous results from XMM-Newton (Behar et al. 2001) and the detection of an Fe XXVI Lyα line in the Suzaku spectrum (Bamba et al. 2017) suggest minor contamination from lower-energy, lower-ionization states of Fe. It is possible that the H-like Fe emission arises from a much hotter plasma that does not produce He-like emission, and the Fe K complex in question is produced by lower-temperature plasma unresolved by both the Suzaku and Hitomi PSF. Although L-shell lines of lower-ionization Fe were not detected by Behar et al. 2001, it is further possible that the L-shell energy band is dominated by the low-temperature swept-up ISM component, hindering detection of faint ejecta lines. We are unable to demonstrate the

validity of our assumptions conclusively with existing X-ray data, and we stress that the discussion that follows assumes the Fe K emission is dominated by He-like Fe.

The best-fitting broadening widths for both Fe K and S K, $\sigma \sim 500 \, \mathrm{km \, s^{-1}}$, greatly exceed thermal broadening at these temperatures. It is unclear whether the constraints on broadening are physical or somehow related to the combination of low statistics and complicated line structure in the thermal model. The addition of broadening simplifies the posterior velocity distribution without greatly changing the 90% credible interval, and we can speculate that if this line broadening is physical, there could be Fe K-emitting material at a range of velocities due to bulk motion, including very high ones. Much better statistics at similar spectral resolution are required to further understand the velocity structure in both Fe K and S K.

These Fe-rich ejecta display very different line-of-sight velocity structures compared to the O-rich ejecta explored in detail in the optical. The O-rich ejecta traced by [O III] $\lambda 5007$ emission have an average blueshifted velocity of $\sim -500 \, \mathrm{km \, s^{-1}}$ with respect to the local LMC when an elliptical shell model is fitted in projected space and velocity (Morse et al. 1995). Vogt and Dopita (2011) confirm this systematic offset, but point out that the complicated spatial structure of the ejecta heavily biases the average velocity of the emission as different clumps interact with the reverse shock at different times. The ring structure of the O-rich ejecta first suggested by Lasker (1980) and confirmed in several successive studies is possibly accompanied by a polar jet associated with a "run-away" knot and the enhanced X-ray emission along the southwestern shell (Vogt & Dopita 2011). It is tempting to speculate that the Fe emission is associated with such a jet, but a more significant detection at higher spatial resolution is required.

The lack of blueshifted emission indicates a highly asymmetric distribution of the Fe-rich ejecta. Such asymmetry is seen morphologically in the ejecta of other core-collapse SNRs, such as Cas A (Grefenstette et al. 2017), G292.2+1.8 (Bhalerao et al. 2015), and W 49 B (Lopez et al. 2013a), and in the more evolved SNRs dominated by shocked ISM/CSM but with Fe knots such as Puppis A (Hwang et al. 2008; Katsuda et al. 2008, 2013). Notably, the Fe ejecta in these remnants are not always centrally concentrated, as would be expected in a typical core-collapse explosion. In Cas A, the mismatch between the shocked Fe ejecta and more concentrated, redshifted ^{44}Ti has been interpreted in light of the SN explosion mechanism involving instabilities such as SASI (Grefenstette et al. 2017). N 132 D is more evolved than Cas A and is perhaps better compared to W 49 B, with which it is comparable in age. The X-ray morphology of N 132 D is more symmetric than W 49 B, and relatively symmetric among core-collapse SNRs in general (Lopez et al.

2011), despite the obvious differences between the bright southern shell and the blown-out northeastern region. This symmetry could indicate a projection effect and an axis of symmetry along the line-of-sight. If N 132 D were observed perpendicular to the direction it is, it might appear more highly asymmetric, like W 49 B.

The origin of the over-ionized plasma is not completely clear. Interestingly, both N 132 D and W 49 B show evidence for overionization of the Fe ejecta (Ozawa et al. 2009; Bamba et al. 2017), suggesting a possible connection between asymmetric ejecta distribution and overionization. In addition, recombining plasma is observed in several mixed-morphology SNRs that are interacting with molecular clouds (e.g., Yamaguchi et al. 2009; Uchida et al. 2015); although the mechanism responsible for the peculiar plasma conditions in these remnants is still unclear, a possible connection is the inhomogeneous medium into which the SNR is expanding. In N 132 D, the entire southern half of the remnant is surrounded in projection by molecular gas, with Mopra 22 m telescope CO data showing that the outer shell is sweeping through the cloud (Banas et al. 1997; Sano et al. 2015). This molecular gas distribution combined with the X-ray emission morphology showing a brighter shell impinging on the cloud in the south suggests that the shock is slowing here due to the cloud, while the fainter shell blowing out toward the north and northeast suggests that the shock is expanding faster here. The detection of both GeV emission (Ackermann et al. 2016) and neutral Fe K (Bamba et al. 2017) from N 132 D further suggest that accelerated protons are interacting with the nearby molecular cloud (Bamba et al. 2017). It is likely that N 132 D is expanding into a highly inhomogeneous medium.

In W 49 B, the recombining plasma is detected on the west side of the remnant whereas the molecular cloud is to the east, suggesting that the dominant cooling mechanism producing the over-ionized plasma is rapid expansion of the inner ejecta (Miceli et al. 2010; Lopez et al. 2013a). A similar density gradient is apparent in N 132 D, however due to the insufficient spatial resolution of either Suzaku or Hitomi we are unable to identify exactly where the recombining plasma is located. Comparing the Fe K map from XMM-Newton (figure 4a of Behar et al. 2001) with the molecular gas map (figure 1b of Sano et al. 2015), we see that the Fe K peak is not in the center of the remnant nor toward the blown-out low-density northeast region, but offset closer to the bright southeastern shell. Since the recombining Fe XXV Heα is the brightest feature seen in this spectral region, this hints that the over-ionized plasma is located near the molecular cloud. With the data currently in hand, and with likely projection effects along the line-of-sight, a firm conclusion is not possible.

It was unfortunate that the first microcalorimeter observation of a thermally dominated SNR was not fully performed due to an attitude control problem. However, this short-exposure observation of N 132 D demonstrates the power of high-spectral-resolution detectors by detecting clear emission features with extremely low photon counts— a similarly short CCD observation would not have detected these features, let alone placed interesting constraints on the velocity. The very low SXS background of ~ 1 event per spectral resolution element per 100 ks is also vital for this result, and it opens the possibility of using slew observations for similar science with similar future instruments. For N 132 D, revealing the Fe ejecta line-of-sight velocity structure, along with its detailed spatial distribution and proper motion, is a vital step to determine its three-dimensional velocity. Future observations with the X-ray Astronomy Recovery Mission (XARM) microcalorimeter, identical in performance to that on Hitomi, will be sufficient to resolve the remnant into two regions spatially and explore in detail the line-of-sight velocity and ionization state for each element. Observations with Athena (Nandra et al. 2013) will also be crucial to constrain the kinematics and ionization state of this SNR more accurately.

6 Conclusions

In this paper, we have presented observations of the LMC SNR N 132 D taken with Hitomi. Using only a short, 3.7 ks observation with the SXS, we detect emission lines of Fe XXV and S XV Heα with only 17 and 16 counts, respectively. Assuming a plausible emission model and prior on the velocity broadening, the Fe line shows a redshift of $800 \, \mathrm{km \, s^{-1}}$ (50–1500 $\mathrm{km \, s^{-1}}$, 90% credible interval) compared to the local LMC ISM, indicating that it likely arises from highly asymmetric ejecta. The S line is consistent with the local LMC standard of rest, shifted by $-65 \, \mathrm{km \, s^{-1}}$ (-450 to $+435 \, \mathrm{km \, s^{-1}}$, 90% credible interval) assuming no broadening, and likely arises from the swept-up ISM. Longer SXI observations produce results consistent with a recent combined Suzaku + NuSTAR spectral analysis, including a recombining thermal plasma component responsible for the Fe XXV Heα emission and constraints on a non-thermal component that dominates at high energies (Bamba et al. 2017). In addition to this first result on SNRs with a microcalorimeter, the observations highlight the power of high-spectral-resolution X-ray imaging instruments in even short exposures.

Author contributions

E. Miller and H. Yamaguchi led this study and wrote the final manuscript along with S. Katsuda, K. Nobukawa,

Acknowledgments

References

Ackermann, M., et al. 2016, A&A, 586, A71

Anders, E., & Grevesse, N. 1989, Geochim. Cosmochim. Acta, 53, 197

Angelini, L., et al. 2016, in Proc. SPIE, 9905, Space Telescopes and Instrumentation 2016: Ultraviolet to Gamma Ray, ed. J.-W. A. denHerder et al. (Bellingham, WA: SPIE), 990514

Arnaud, K. A. 1996, in ASP Conf. Ser., 101, Astronomical Data Analysis Software and Systems V, ed. G. H. Jacoby & J. Barnes (San Francisco: ASP), 17

Bamba, A., et al. 2018, Apj, 854, 71

Banas, K. R., Hughes, J. P., Bronfman, L., & Nyman, L.-Å. 1997, ApJ, 480, 607

Bautz, M. W., et al. 2009, PASJ, 61, 1117

Behar, E., Rasmussen, A. P., Griffiths, R. G., Dennerl, K., Audard, M., Aschenbach, B., & Brinkman, A. C. 2001, A&A, 365, L242

Bhalerao, J., Park, S., Dewey, D., Hughes, J. P., Mori, K., & Lee, J.-J. 2015, ApJ, 800, 65

Blair, W. P., et al. 2000, ApJ, 537, 667

Borkowski, K. J., Hendrick, S. P., & Reynolds, S. P. 2007, ApJ, 671, L45

Canizares, C. R., Flanagan, K. A., Davis, D. S., Dewey, D., & Houck, J. C. 2001, in ASP Conf. Ser., 234, X-ray Astronomy 2000, ed. R. Giacconi et al. (San Francisco: ASP), 173

Cash, W. 1979, ApJ, 228, 939

Danziger, I. J., & Dennefeld, M. 1976, ApJ, 207, 394

de Vries, C. P., et al. 2018, J. Astron. Telesc. Inst. Syst., 4, 011204

Eckart, M. E., et al. 2016, in Proc. SPIE, 9905, Space Telescopes and Instrumentation 2016: Ultraviolet to Gamma Ray, ed. J.-W. A. den Herder et al. (Bellingham, WA: SPIE), 99053W

Favata, F., Vink, J., Parmar, A. N., Kaastra, J. S., & Mineo, T. 1997, A&A, 324, L45

Foster, A. R., Ji, L., Smith, R. K., & Brickhouse, N. S. 2012, ApJ, 756, 128

Fujimoto, R., et al. 2016, in Proc. SPIE, 9905, Space Telescopes and Instrumentation 2016: Ultraviolet to Gamma Ray, ed. J.-W. A. den Herder et al. (Bellingham, WA: SPIE), 99053S

Gehrels, N. 1986, ApJ, 303, 336

Grefenstette, B. W., et al. 2014, Nature, 506, 339

Grefenstette, B. W., et al. 2017, ApJ, 834, 19

H.E.S.S. Collaboration 2015, Science, 347, 406

Hitomi Collaboration 2016, Nature, 535, 117

Hitomi Collaboration 2018, PASJ, 70, 12

Hughes, J. P. 1987, ApJ, 314, 103

Hughes, J. P., et al. 2014, arXiv:1412.1169

Hughes, J. P., Hayashi, I., & Koyama, K. 1998, ApJ, 505, 732

Hwang, U., Hughes, J. P., Canizares, C. R., & Markert, T. H. 1993, ApJ, 414, 219

Hwang, U., & Laming, J. M. 2012, ApJ, 746, 130

Hwang, U., Petre, R., & Flanagan, K. A. 2008, ApJ, 676, 378

Janka, H.-T., Melson, T., & Summa, A. 2016, Annu. Rev. Nuclear and Particle Sci., 66, 341

Kamitsukasa, F., et al. 2014, PASJ, 66, 64

Katsuda, S., Mori, K., Tsunemi, H., Park, S., Hwang, U., Burrows, D. N., Hughes, J. P., & Slane, P. O. 2008, ApJ, 678, 297

Katsuda, S., Ohira, Y., Mori, K., Tsunemi, H., Uchida, H., Koyama, K., & Tamagawa, T. 2013, ApJ, 768, 182

Kelley, R. L., et al. 2016, in Proc. SPIE, 9905, Space Telescopes and Instrumentation 2016: Ultraviolet to Gamma Ray, ed. J.-W. A. den Herder et al. (Bellingham, WA: SPIE), 99050V

Kilbourne, C. A., et al. 2018, J. Astron. Telesc. Inst. Syst., submitted

Lasker, B. M. 1980, ApJ, 237, 765

Lopez, L. A., Pearson, S., Ramirez-Ruiz, E., Castro, D., Yamaguchi, H., Slane, P. O., & Smith, R. K. 2013a, ApJ, 777, 145

Lopez, L. A., Ramirez-Ruiz, E., Castro, D., & Pearson, S. 2013b, ApJ, 764, 50

Lopez, L. A., Ramirez-Ruiz, E., Huppenkothen, D., Badenes, C., & Pooley, D. A. 2011, ApJ, 732, 114

Mathewson, D. S., Ford, V. L., Dopita, M. A., Tuohy, I. R., Long, K. S., & Helfand, D. J. 1983, ApJS, 51, 345

Miceli, M., Bocchino, F., Decourchelle, A., Ballet, J., & Reale, F. 2010, A&A, 514, L2

Morse, J. A., et al. 1996, AJ, 112, 509

Morse, J. A., Winkler, P. F., & Kirshner, R. P. 1995, AJ, 109, 2104

Nakajima, H., et al. 2018, PASJ, 70, 21

Nandra, K., et al. 2013, arXiv:1306.2307

Noda, H., et al. 2016, in Proc. SPIE, 9905, Space Telescopes and Instrumentation 2016: Ultraviolet to Gamma Ray, ed. J.-W. A. den Herder et al. (Bellingham, WA: SPIE), 99053R

Nomoto, K., Tominaga, N., Umeda, H., Kobayashi, C., & Maeda, K. 2006, Nucl. Phys. A, 777, 424

Ozawa, M., Koyama, K., Yamaguchi, H., Masai, K., & Tamagawa, T. 2009, ApJ, 706, L71

Park, S., Hughes, J. P., Slane, P. O., Burrows, D. N., Gaensler, B. M., & Ghavamian, P. 2007, ApJ, 670, L121

Plucinsky, P. P., Foster, A., Gaetz, T., Jerius, D. H., Patnaude, D., Edgar, R. J., Smith, R. K., & Blair, W. P. 2016, Am. Astron. Soc. Meeting Abstr., 227, 238.07

Porter, F. S., et al. 2016a, in Proc. SPIE, 9905, Space Telescopes and Instrumentation 2016: Ultraviolet to Gamma Ray, ed. J.-W. A. den Herder et al. (Bellingham, WA: SPIE), 99050W

Porter, F. S., et al. 2016b, J. Low Temperature Phys., 184, 498

Sano, H., et al. 2015, in ASP Conf. Ser., 499, Revolution in Astronomy with ALMA: The Third Year, ed. D. Iono et al. (San Francisco: ASP), 257

Sutherland, R. S., & Dopita, M. A. 1995, ApJ, 439, 365

Takahashi, T., et al. 2016, in Proc. SPIE, 9905, Space Telescopes and Instrumentation 2016: Ultraviolet to Gamma Ray, ed. J.-W. A. den Herder et al. (Bellingham, WA: SPIE), 99050U

Uchida, H., Koyama, K., & Yamaguchi, H. 2015, ApJ, 808, 77

Ueda, Y., et al. 1999, ApJ, 518, 656

Vogt, F., & Dopita, M. A. 2011, Ap&SS, 331, 521

Westerlund, B. E. 1990, A&A Rev., 2, 29

Woosley, S. E., & Heger, A. 2007, Phys. Rep., 442, 269

Xiao, X., & Chen, Y. 2008, Adv. Space Res., 41, 416

Yamaguchi, H., et al. 2014, ApJ, 785, L27

Yamaguchi, H., Ozawa, M., Koyama, K., Masai, K., Hiraga, J. S., Ozaki, M., & Yonetoku, D. 2009, ApJ, 705, L6